Master of Physics

Anomalous Nernst Effect in Epitaxially Grown Mn_3Sn Thin Films

Department of Physics and Laboratory for Spin-Orbitronic Devices,

University of Ulsan, Ulsan 44610, Republic of Korea

Ullah Asif

Anomalous Nernst Effect in Epitaxially Grown Mn_3Sn Thin Films

Supervisor: Sanghoon Kim

A Dissertation

Submitted to
the Graduate School of the University of Ulsan
In partial Fulfillment of the Requirements
for the Degree of

Master of Physics

by

Ullah Asif

Department of Physics
Laboratory for Spin-Orbitronic Devices
University of Ulsan, Ulsan 44610, Korea

April 2024

Anomalous Nernst Effect in Epitaxially Grown Mn_3Sn Thin Films

This is to declare that the dissertation

submitted by Ullah Asif is approved officially.

조 성래

Committee Chair: Prof. Sunglae Cho

Department of Physics, University of Ulsan

Committee Member: Prof. Sonny Rhim

Department of Physics, University of Ulsan

Committee Member and Supervisor: Prof. Sanghoon Kim

Department of Physics, University of Ulsan

Department of Physics and Laboratory for Spin-Orbitronic Devices

University of Ulsan, Ulsan 44610, Republic of Korea

June 2024

Acknowledgements

First, I must express my sincere gratitude to Professor Sanghoon Kim. I feel fortunate and honored to have completed my master's degree under the supervision of such an inspirational Professor. His zeal for research in Physical science is contagious and is truly motivational for young physicists. The way he encourages his students and the kind of belief he has in them is next to none. I greatly appreciate all his time, discussions, and valuable ideas that helped me a lot to improve my experimental skills and concepts. He helped me understand, consciously or unconsciously, the essence of experimental physics.

I am also grateful to the faculty members in the Department of Physics for their valuable insights, comments, and suggestions that have helped me to improve the quality of my work. Their teachings, encouragement, and mentorship have been a great source of inspiration for me.

My heartful thanks to the lab Alumni and all the current members who not only helped me in every situation but also guided me. I feel lucky to work in such a healthy and friendly environment. I would like to extend my gratitude to my colleagues and friends for their encouragement, motivation, and assistance during this journey. Their invaluable contributions, both academically and personally, have made this thesis possible.

I am deeply grateful to my family for their unconditional love, support, and encouragement. Their unwavering belief in me has been a constant source of strength and inspiration.

Thank you.

ASIF ULLAH

Abstract

New trends in next-generation magnetic information storage focus on controlling the magnetic domain wall propagation and positioning. Ferromagnetic as well as antiferromagnetic materials have gained attention for energy harvesting and memory devices, particularly in the field of spin caloritronic. The Seebeck effect, on which the conventional thermoelectric devices are working generate thermoelectric voltage longitudinally to the temperature gradient. However, for the application, this effect has a shortcoming of the heat source part of the electrical circuit. To surmount this challenge, multiterminal thermoelectric devices have freedom of spatial separation of heat reservoir from the electrical circuit.

Our study explores the potential implementation of the Anomalous Nernst Effect, in which a temperature gradient ($\nabla \mathbf{T}$) and magnetic field ($\mathbf{B}$) perpendicular to each other produces a transverse thermoelectric voltage signal. Epitaxially grown Mn_3Sn thin films (30 nm) on MgO (110) substrates with a Tungsten (W) seed layer (7 nm) and Tantalum (Ta) capping layer (3 nm) serve as the device structure. Hall bar-shaped devices were fabricated using photolithography and ion milling processes. Then, a separate 50 nm thick tungsten heater was fabricated by W sputtering using DC magnetron sputter method and lift-off process across the longitudinal contact of the Hall bar at each end. The sample layout and geometry of the on-chip heaters enables the direct measurements of the Anomalous Hall Effect and Anomalous Nernst Effect. By applying out-of-plane magnetic field and current through the heater line, we measure the Nernst voltage signals from the nearest voltage contacts. All the measurements were performed at room temperature using the Keithly 6221 source meter, Keithley 2182A as a voltmeter and an electromagnetic.

Antiferromagnetic materials, having non-collinear spin configuration, lead to generation of large Berry curvature via spin-orbit coupling gained interest due to their thermoelectric magneto-transport effects. This Berry curvature arising from the magnetic multipole plays an important role not only in Anomalous Hall effect but also in Anomalous Nernst effect. Breaking of time reversal and inversion symmetry along with the translation and time reversal leads to the Integral nonzero value, these are the intrinsic contributors to the AHE and ANE. However, the AHE arises from all the occupied bands while the ANE originates only from the occupied bands of the Fermi level.

Unlike conventional thermoelectric devices, Anomalous Nernst devices eliminate the need for p-type and n-type materials, simplifying technological integration. This work not only highlights the development of multi-terminal devices but also expands the understanding of Anomalous Nernst Effect in antiferromagnetic materials which leads to the future innovations and applications in energy harvesting and memory devices.

Outline

List of figures

1. Introduction

In our society, the capacity for storing data has significantly expanded to accommodate the ever-growing volume of information being generated. Concurrently, with time reduction in size of memory devices is observed. This advancement in data storage capacity in reduced size devices has facilitated convenient storage and information exchange, for instance, audio and images in mobile phones, laptops, and social media platforms. A significant factor contributing to this technological progress is the manipulation of electron spin, leading to the emergence of spintronics as a prominent field of research and technology. A pivotal advancement in spintronics was the discovery in the shape of giant magnetoresistance. This mechanism transformed the basic function of memory devices, substituting the traditional concept of collective magnetization of localized spins in ferromagnetic layers with electronic conduction that relies on the electrons spin state. Binary states 0 and 1 are used to encode digital information, which correspond to distinct configurations of spin.

Spintronics manipulates the intrinsic spin of the electron, its associated magnetic moment, and its fundamental electronic charge. The main idea is to use the electron's spin as well as its charge. Electrons can spin in two directions: spin-up and spin-down also known as clockwise and anti-clockwise spin.

Spintronic is based on the three conventional information carriers: an electron charge, an electron spin, and a photon. These carriers represent three major fields: data processing with electron transport, data storage with an assembly of spin, and data transfer via optical connections as shown in Figure1. Spintronics provides high-speed, high-power lasers, lower threshold current, high-density logic, low-power, electronic memory devices, and optoelectronic devices. In such devices, the interaction of the spin of electrons and orbital angular momentum is used. For example, the hard disk drive (a magnetic device using a spin quantum number) was invented by IBM in 1956.

Development in nanofabrication technology has also benefitted the magnetic community in the semiconductor area.

Characteristics of magnetic devices:

- Strong dependence of electron transport properties on the atomic smoothness of their surfaces and interface.
- Magnetic materials have low resistivity for electron transport of the order (10-7-10-8) Ω.m at room temperature.
- Spin diffusion length (distance over which an electron can keep the memory of its spin) is typically ~5nm for ferromagnetic and ~300nm for nonmagnetic materials.
- Spin polarization is the key parameter to characterize the device and system activity.
- Spin polarization controls the efficiency of spin-polarized electron transport.
- Conduction electrons in a conductor or spin-wave propagation across local magnetic moments in an insulator is used for spin polarization transfer.

Characteristics of semiconducting devices:

- Transport properties are controlled by a depletion layer formed at their interfaces against a metallic layer.
- Depletion layer has a thickness between a few nm (Indium arsenide InAs) and a few μm (Gallium arsenide GaAs).
- Semiconductors have high resistivity for electron transport of the order (10-5-108) Ω.m at room temperature.
- Spin diffusion length is typically ~1,000nm.
- Doping density is the key parameter to characterize the device and system activity.
- Doping density controls the diffusion length and resistivity.

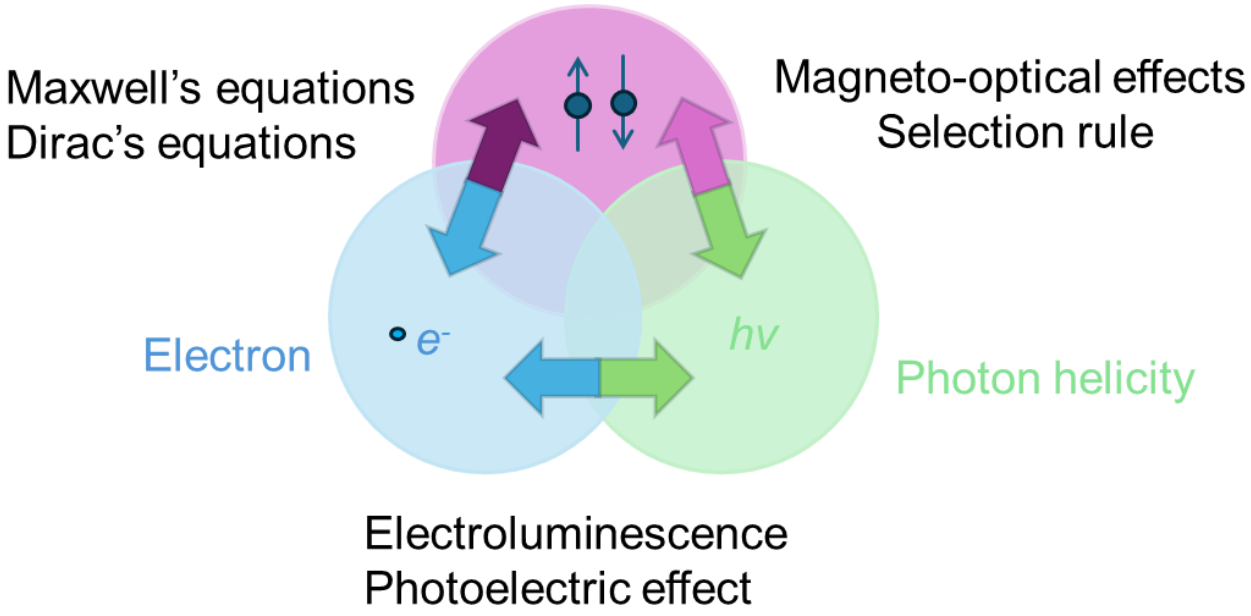

Figure 1. Convergence of spintronics phenomena.

2. Theoretical Background

2.1 Seebeck effect

In 1821, Thomas Seebeck made a significant discovery regarding the behavior of unsimilar materials when subjected to varying temperatures. By joining together two different materials, such as copper and bismuth wires, and maintaining their junctions at differing temperatures (designated as T and $T + \Delta T$), he observed the emergence of a voltage difference (ΔV), which was found to be directly proportional to the temperature variance (ΔT). This phenomenon, known as the Seebeck effect, shows an intrinsic characteristic of materials, which can be mathematically described by an equation given below [1]:

$$\vec{J} = \sigma(\nabla V - S\nabla T) \tag{1}$$

In equation (1), $\vec{J}$ denotes the electrical current density whereas σ represents the electrical conductivity. When a temperature gradient denoted by ∇T is applied in the x-direction, it initiates charge carriers' movement in the material, causing them to diffuse towards the boundaries of the material and accumulate there. This accumulation gives rise to an electric field $E_x = \nabla V$, which induces a charge carriers drift countering the current driven by ∇T_x. Consequently, $\vec{J}$ which denotes the total current density reaches zero, as described by the equation $\sigma\nabla V_x - \sigma S\nabla T_x = 0$. This balance indicates that the Seebeck coefficient S_x, defined as the ratio between the electric field and temperature gradient denoted mathematically as $S_x = \nabla V_x/\nabla T_x$. It plays an important role in maintaining equilibrium. This process is illustrated in detail in Figure 2, representing the phenomenon known as the Seebeck effect, where the temperature gradients lead to the generation of electric fields and subsequent charge carrier movements, finally effecting the conductivity of the material.

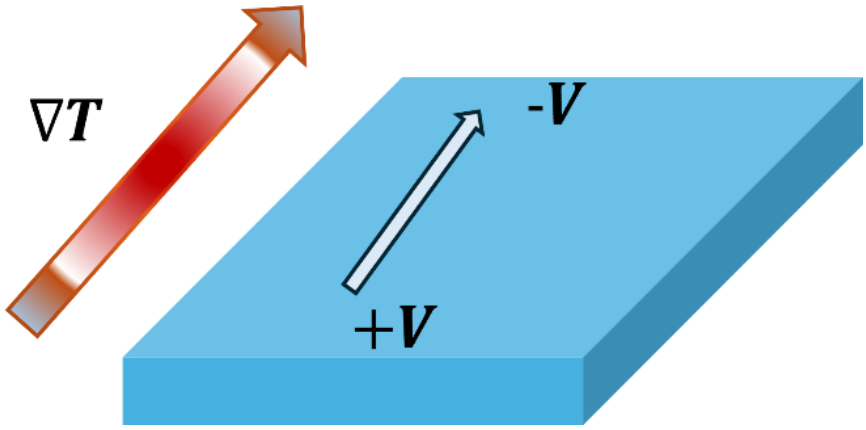

Figure 2. Schematic diagram of the Seebeck effect.

The Seebeck effect arises from the concept that the conductivity of electrons is affected by their energy levels. According to Fermi-Dirac statistics, the distribution of electrons across energy states, characterized by the density of states $g(E)$, follows a $\sqrt{E}$ scaling. At high temperatures, electrons migrate towards high energy states. It is due to temperature dependency, resulting in an elevated average energy per electron

compared to those at cooler temperatures. As a result, there exists a net flow of energy as electrons move from the hotter to the colder regions, carrying with them more energy than those moving in the opposite direction. This phenomenon essentially shows the electrons' thermal conductivity. If the high and low energy electrons have the same conductivity, it leads to trivial charge currents, hence no net charge movement occurs. In contrast, when electrons with varying energy levels exhibit distinct conductivities, a net charge diffusion arises. In equilibrium state, this diffusion process is obstructed by the initiation of an electric field, known as Seebeck effect, which hinders further diffusion[2].

2.2 Method of spin polarization:

In non-magnetic materials, the methods of spin polarization as shown in Figure 3 are given below:

I. Spin injection from a ferromagnetic material.
II. Appling magnetic field.
III. Appling electric field.
IV. Electromagnetic wave introduction.
V. Zeeman splitting.
VI. Spin motive force.
VII. Thermal gradient.
VIII. Mechanical rotation.

Spin injection (transfer of spin angular momentum from a FM to non-FM) from a FM (e.g., Fe. CO, Ni, and Gd), half-metallic ferromagnets (HMF) and dilute magnetic semiconductors (DMS) to a non-magnetic metal or semiconductor through an ohmic contact or a tunnel barrier is the most common method used.

The efficiency of the spin current generation is very important for the device applications defined as:

$$\eta = \frac{Generated\ spin\ current}{introduced\ energy} \tag{2}$$

For the spin current generated from the charge current by the spin Hall effect the following equation can be used,

$$\eta = \frac{Generated\ spin\ current\ denisty}{Electron\ charge\ current\ density} = \frac{j_s}{j_c} \tag{3}$$

The efficiency (η) of the system with interfaces between a FM and a NM is lower than those with no interfaces.

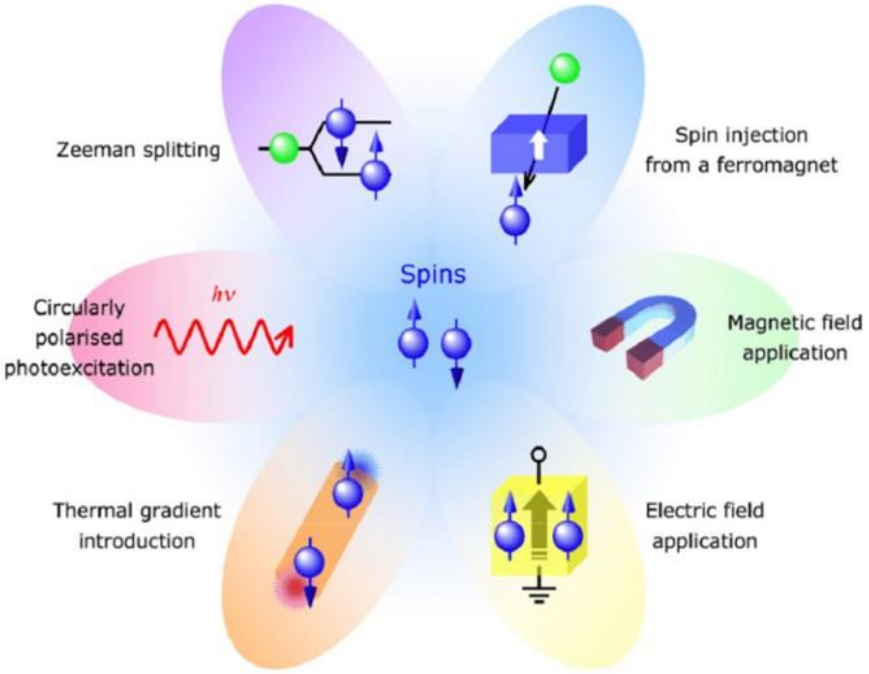

Figure 3. Schematic of major methods for spin polarized current.

2.3 Ordinary Hall Effect:

In 1879, Edwin H. Hall proposed a phenomenon known as the ordinary Hall effect (OHE). This effect describes the generation of a small transverse electric field (E_H) when a primary current density (I_D) passes through a material while applying a magnetic field (B_Z). The relationship between these variables is such that the magnitude of the electric field is proportional to the product of two quantities, namely current density, and magnetic flux. In simpler terms, the OHE suggests that when an electric current flows through a material subjected to a magnetic field, it creates a perpendicular electric field[3]. A mathematical equation expresses this relationship as given below:

$$E_H = RI_D B_Z \tag{4}$$

The Hall effect, described by the Hall coefficient R, illustrates a linear response where transverse electric field and applied magnetic field are directly proportional to each other as shown in Figure 4.

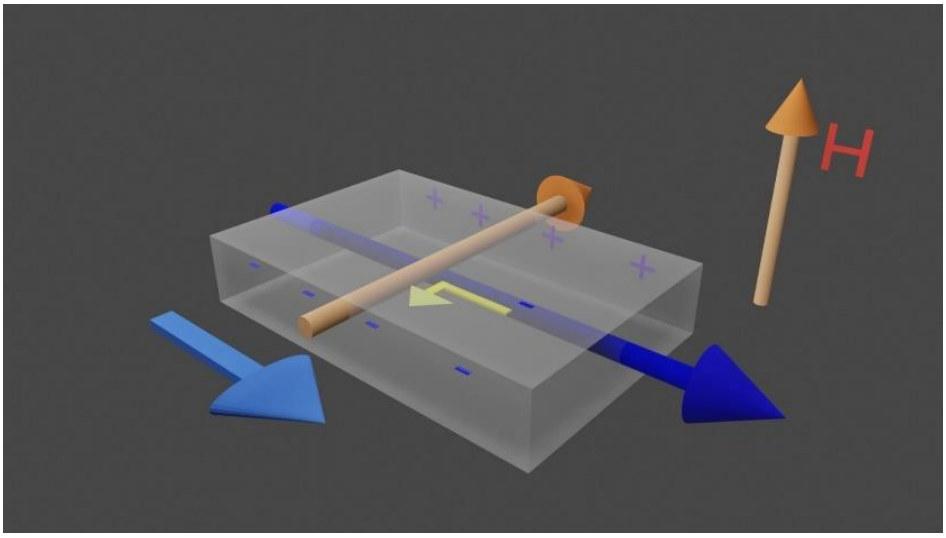

Figure 4. Schematic diagram for Ordinary Hall Effect.

2.4 Anomalous Hall Effect:

In ferromagnetic materials, there exists a phenomenon namely Anomalous Hall Effect AHE. Unlike the ordinary Hall effect, the response in AHE is not directly proportional to the applied magnetic field due to spontaneous magnetization. This leads to the emergence of a Hall resistivity (ρ_{xy}) that cannot be only attributed to the ordinary Hall effect. Instead, the Hall resistivity in ferromagnetic materials is empirically shown as the output resulting from the addition the anomalous Hall effect resistivity (ρ_{xy}^{AHE}) and the ordinary Hall effect resistivity (ρ_{xy}^{OHE}). This empirical relationship represents both the conventional and non-linear responses observed in ferromagnetic systems. This relationship is mathematically expressed as given below:

$$\rho_{xy} = (\rho_{xy}^{AHE}) + (\rho_{xy}^{OHE}) \tag{5}$$

$$\rho_{xy} = R_O B_Z + R_S M \tag{6}$$

In this equation, B_Z represents the applied magnetic field, while M denotes magnetization. Additionally, R_O and R_S stand for the ordinary and anomalous Hall coefficients, respectively. Magnetization and Hall resistivity relationship was first marked by Smith and Pugh, which later resulted in the discovery of the AHE [4], [5].

The AHE has its basis in two distinct mechanisms namely intrinsic and extrinsic Hall effects. Karplus and Luttinger identified the intrinsic AHE. They focused on the basic spin-orbit interactions experienced by moving, spin-polarized electrons within a material. Their study suggested that these intrinsic interactions result in electrons acquiring a group velocity when subjected to an external electric field[6] . In simpler terms, intrinsic AHE arises from the intrinsic properties of a material's electronic structure, particularly how the interaction between electron spin and orbital motion influences their behavior under external conditions such as an applied electric field.

For a considerable period, it was widely believed that the anomalous Hall conductivity (AHC) correlates directly with the magnetization in a sample. Consequently, any ferromagnetic material exhibits an AHE, while it remains absent in antiferromagnets due to cancellation of magnetic sublattices which result in $(M = 0)$.Therefore, the AHE is considered as a significant indicator in ferromagnets or ferrimagnets for finite magnetization[7], [8]. Yet, recent findings have shown that the inherent contribution to the anomalous Hall effect (AHE) is not exclusively determined by a material's magnetization, but from the integration of net Berry curvature.

The arrangement of Berry curvature within materials reflects their band structure, which consequently determines their topological characteristics. The absence of time-reversal symmetries and the presence of a finite net Berry curvature is an important requirement for a non-zero AHC[6]. Remarkably, time-reversal symmetries cause the local Berry curvature to reverse its sign in the Brillouin Zone (BZ) when the momentum vector sign is reversed. By utilizing appropriate manipulations of symmetries and band structures, Berry curvature and intrinsic AHE can be controlled independently of the magnetization's finite value.

Concluding these considerations, a substantial AHC has been predicted in noncollinear antiferromagnetic systems such as Mn_3Ir, Mn_3Ge, and Mn_3Sn[9], [10]. This prediction has been subsequently validated experimentally in Mn_3Ge[11] and Mn_3Sn. Moreover, recent discoveries have unveiled a substantial intrinsic AHE in magnetic Weyl semimetals with broken time-reversal symmetry, which depends on the separation of Weyl nodes in momentum space. In these materials, the Weyl point serves as the monopoly of Berry curvature, allowing assignment of a topological invariant, the Chern number, to each Weyl node. Consequently, the AHC can be modulated through symmetry and topological band structure considerations, irrespective of net magnetic moments. The schematic in Figure 5 illustrates the AHE phenomenon.

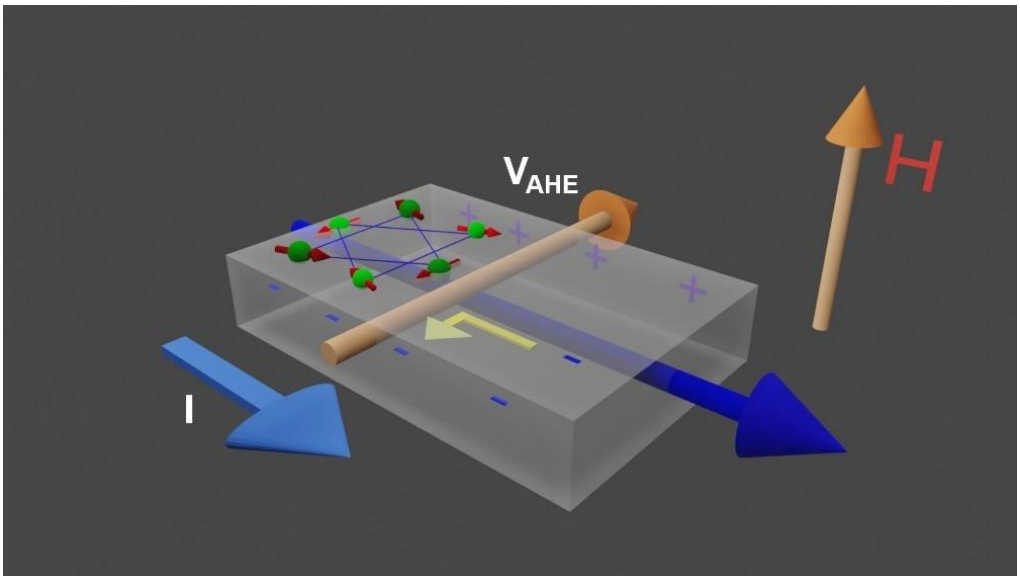

Figure 5. Schematic diagram for Anomalous Hall Effect.

2.5 Anomalous Nernst Effect:

The anomalous Nernst effect (ANE) is a phenomenon that occurs with a temperature gradient in a ferromagnetic conductor generating a transverse voltage perpendicular to both magnetization and heat current as shown in Figure 6. This effect can be observed in non-ferromagnetic materials including antiferromagnetic materials such as Mn_3Sn as well as ferromagnets. The anomalous Nernst effect (ANE) serves as the thermal analog of the anomalous Hall effect (AHE)[12]. It is a significant phenomenon in research area related to spin-caloritronic, observed in experiments as a transverse voltage generated in a magnetic material under a thermal gradient[13].

$$E = Q_s \mu_o M \times (-\nabla T) \tag{7}$$

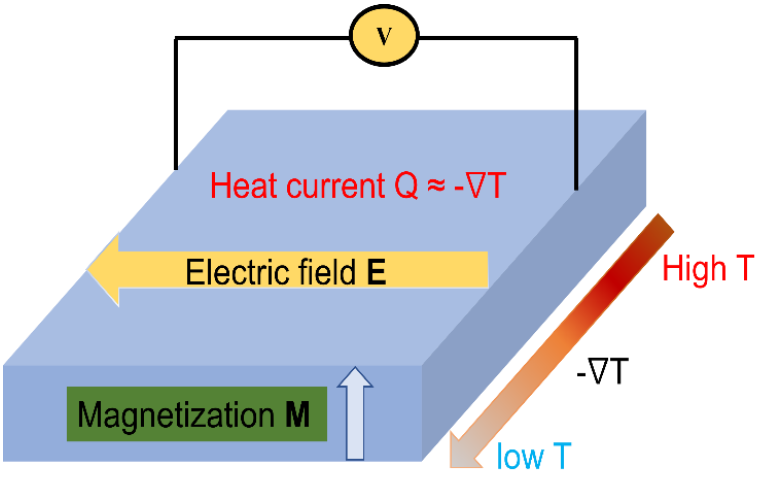

Figure 6. Diagram for Anomalous Nernst Effect.

Where Q_s is the anomalous Nernst coefficient and μ_o is vacuum permeability. Initially, it was thought that there exists a direct relationship between ANE and magnetization. However, recent works indicate that the effect of Berry curvature may have a more significant influence. Extensive debates have surrounded the exact origins of both the anomalous Hall effect (AHE) and anomalous Nernst effect (ANE)[10], [14]. Generally, the contributions from extrinsic and intrinsic factors are well understood. Certain materials have been suggested to exhibit a predominant influence of the anomalous Nernst effect (ANE) by the collective net Berry curvature of all bands near the Fermi level[15]. Additionally, the relationship between the AHE and ANE can be understood through the Mott relation[16].

$$\alpha_{xy} = -\frac{(\pi k_B)^2}{3e} \frac{\partial \sigma_{xy}(\epsilon)}{\partial \epsilon} T \,|_{\epsilon=\mu} \tag{8}$$

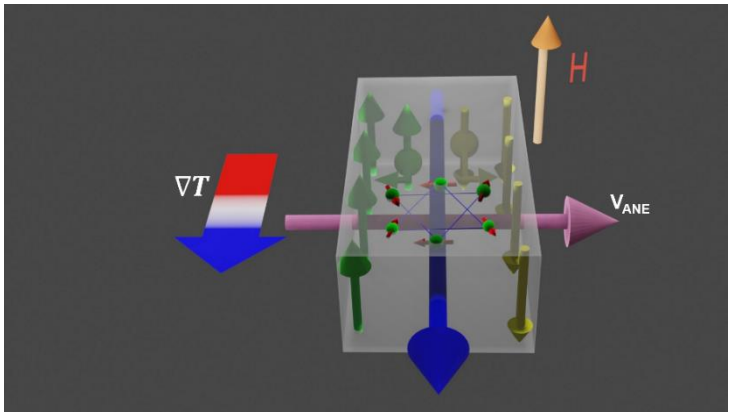

Figure 7. Schematic diagram for Anomalous Nernst Effect.

Experimental findings have shown that the Mn_3Sn demonstrates a significant anomalous Hall effect (AHE). It's important to note that the AHE is derived from integrating the Berry curvature across all occupied bands, while the anomalous Nernst effect (ANE) specifically based on the Berry curvature at the Fermi level (EF)[17], [18]. Therefore, the presence of a substantial AHE doesn't necessarily show a notable ANE. Hence the measurement of ANE be useful to represents the Berry curvature spectra around the Fermi level to verify the Weyl metals nowadays proposed for the Mn_3Sn[19].

By using the theoretical approach, the efficiency of the anomalous Nernst device can be calculated from the anomalous Nernst coefficient value which is primary challenge for the anomalous Nernst device that the material exhibits high value of the anomalous Nernst coefficient. Generally, the anomalous Nernst coefficient value is proportional to the derivative of anomalous Hall conductivity as an energy function [20], [21] The anomalous Hall conductivity is determined by the extrinsic and intrinsic contribution. In [22], the anomalous Hall conductivity is calculated as:

$$\sigma_{xy}^{A} = -\frac{e^2}{\hbar}\sum_n \int \frac{dk}{(2\pi)^3}\Omega_{n,xy}(k) f_{nk} \tag{9}$$

where f_{nk} is the Fermi-Dirac distribution function with the band index n and the wave vector k. e denotes the elementary charge and $\hbar$ is the reduced Planck constant. $\Omega_{n,xy}$ presents the Berry curvature. The integral was performed across the whole Brillouin zone for all bands below E_F.

The Berry curvature is given by the relation:

$$\Omega_{xy} = \sum_{m\neq n} \frac{\left\langle n\left|\frac{\partial H}{\partial k_x}\right|m\right\rangle\left\langle m\left|\frac{\partial H}{\partial k_y}\right|n\right\rangle - \left\langle n\left|\frac{\partial H}{\partial k_y}\right|m\right\rangle\left\langle m\left|\frac{\partial H}{\partial k_x}\right|n\right\rangle}{(\epsilon_n - \epsilon_m)^2} \tag{10}$$

where m and n are the eigenstates and ϵ are the eigen energies of the Hamiltonian H.

From the anomalous Hall conductivity and Berry curvature the anomalous Nernst conductivity is calculated as in [22],

$$\alpha_{yx}^{A} = \frac{e}{T\hbar}\sum_n \frac{dk}{(2\pi)^3}\Omega_{n,yx}(k)\{(\varepsilon_{nk} - \mu) f_{nk} + k_B T \ln[1 + e^{-\beta(\epsilon_{nk}-\mu)}]\} \tag{11}$$

where ϵ_{nk} is the band energy, k_B is the Boltzmann constant and $\beta = k_B T$.

3. Experimental Setup and Preparation of Samples

This chapter provides a comprehensive overview of the experimental procedures implemented throughout this research. Beginning with sample growth, detailed discussions on the methodologies of photolithography and ion milling are presented. Subsequently, the utilization of X-ray diffraction techniques for the structural characteristics and quality of the samples. Finally, a detailed explanation of the measurement of the Anomalous Nernst coefficient S_{ij} is presented, with a specific emphasis on its significance in examining the thermoelectric characteristics displayed by the thin film of Mn_3Sn materials under study.

3.1 Preparation of Sample:

3.1.1 Physical vapor deposition:

Physical vapor deposition (PVD) methods are used for deposition of thin films in experimental research. PVD involves energy as an input to a material in solid state to transform into vapor phase which condenses on material surface in an ultrahigh vacuum (UHV) environment that typically maintains a high pressure of around 1x10-8 mbar and are commonly employed in fabrication processes of semiconductor material.

Magnetron sputtering is a subset of PVD. It uses a background gas in an ultraclean UHV environment. This system typically utilizes argon Ar gas at low pressures. Argon ions, carrying a positive charge, are injected towards the negatively charged target material. As a result of this interaction, atoms from the solid target material move towards the substrate. This process facilitates the deposition of material on the surface of substrate in the vacuum chamber, resulting in the growth of the target material.

In this study, Epitaxially grown Mn_3Sn thin films (30 nm) on MgO (110) substrates with a Tungsten (W) seed layer (7 nm) and Tantalum (Ta) capping layer (3 nm) were deposited using DC magnetron sputtering and a separate heater across the device is also being deposited using same system. Figure 8 shows the different targets positions and the inside view of the chamber.

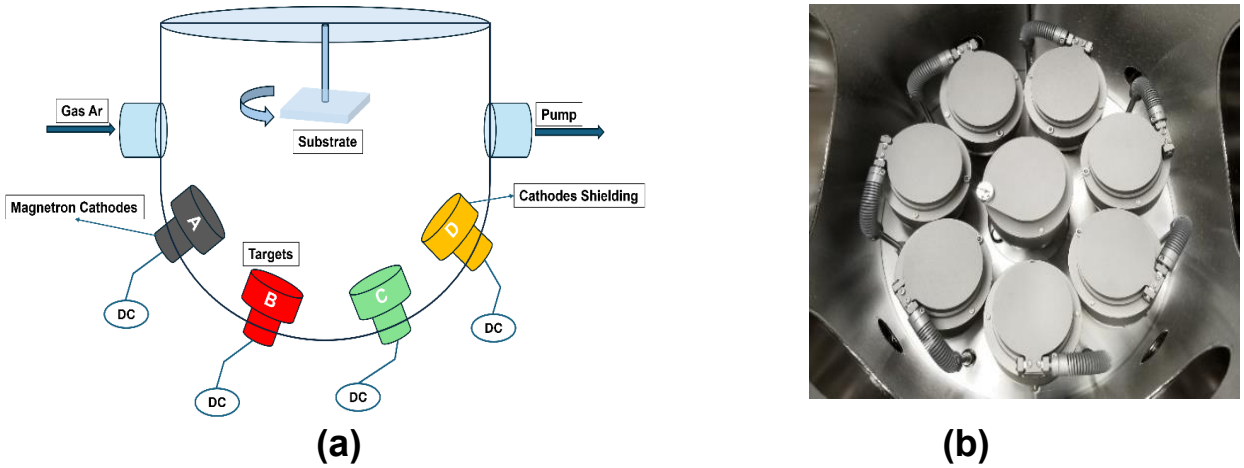

Figure 8. (a) Schematic and **(b)** Inside view of sputtering chamber.

3.1.2 Mask design:

For fabricating the Anomalous Nernst devices in the Mn_3Sn, we must design of the device in detail at the micrometer scale. First in the laboratory, the CAD file is designed for specific geometry shown in Figure 9 and is used for the Anomalous Nernst device and AHE.

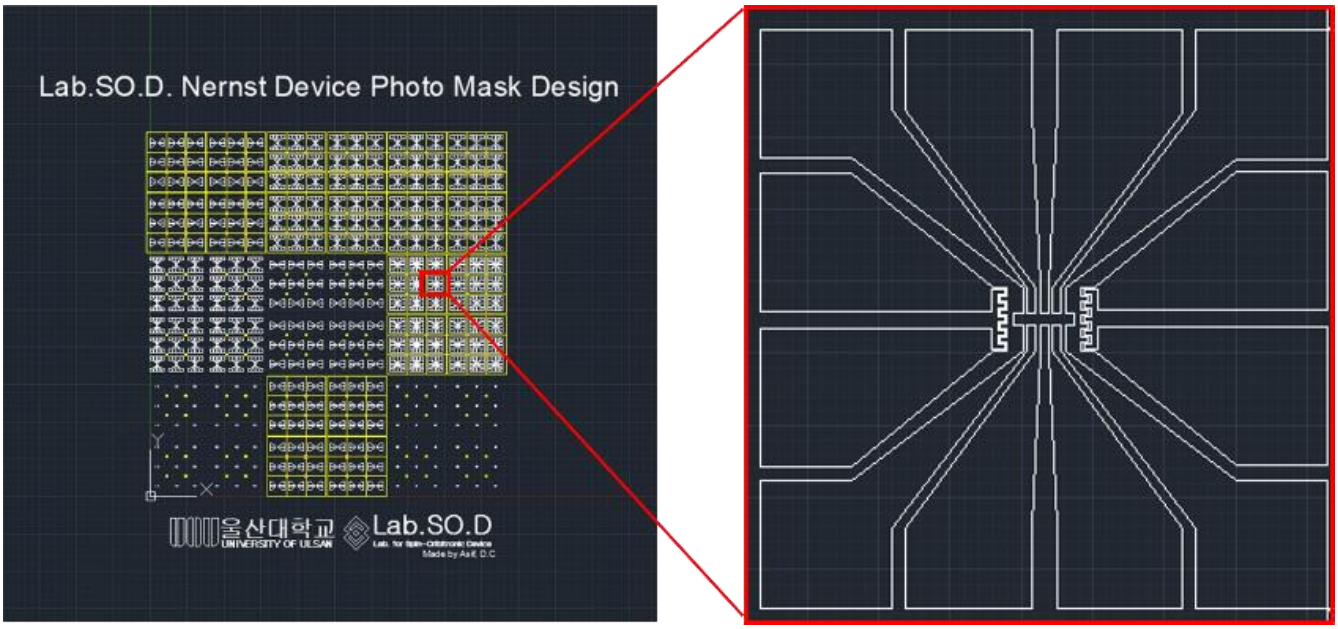

Figure 9. CAD diagram for ANE Mask.

3.2 Photolithography:

In the study of micro and nanoscale materials structuring and patterning, photolithography serves as a fundamental nanofabrication technique widely used across the semiconductor and engineering disciplines. It works on the illumination of a substrate coated with a light-sensitive material, typically called a photoresist, to copy a pattern from a mask onto the substrate surface. Photolithography enables us to copy precise and reproducible structures, ranging from sub-micrometer to nanoscale dimensions, through multiple chemical and physical processes performed on the substrate, including soft baking, exposure, hard baking, development, and etching. This method finds application across various fields such as microelectronics, nanophotonic, microfluidics, and biotechnology, facilitating the development of advanced systems and devices with enhanced performance.

The different types of photolithography which are commonly used are[23]:

3.2.1 Optical Photolithography:

Optical photolithography, widely favored in various industries such as semiconductor manufacturing and microelectronics, stands out as the predominant method. This technique involves transferring a pattern from a mask onto a photosensitive substance applied to a substrate, typically employing optical radiation, often in the ultraviolet (UV) or visible spectrum.

3.2.2 Extreme Ultraviolet Lithography:

Extreme Ultraviolet (EUV) Lithography represents a significant advancement beyond optical lithography, offering superior resolution and finer feature sizes. By harnessing extreme ultraviolet light, with wavelengths spanning 10–14 nanometers, this cutting-edge technique holds promise for revolutionizing semiconductor fabrication processes.

3.2.3 X-ray Lithography:

X-ray Lithography employs X-rays with wavelengths ranging from 0.1 to 10 nanometers to imprint patterns onto a substrate. This advanced technique finds specialized applications in the fabrication of high-density interconnects and microelectromechanical systems (MEMS), showcasing its versatility and precision in diverse technological fields.

3.2.4 Electron Beam Lithography:

Electron Beam Lithography employs a focused electron beam to directly inscribe designs onto a substrate. Renowned for its remarkable resolution, this technique finds widespread use in research laboratories and specialized applications, particularly in crafting nanostructures and devices with unparalleled precision.

3.2.5 Nanoimprint Lithography:

Nanoimprint Lithography involves imprinting a pattern onto a photosensitive substance deposited on a substrate using a template with intricate designs. This technique is renowned in nanofabrication for its simplicity, cost-effectiveness, and ability to achieve exceptional resolution, making it a popular choice in various applications.

3.2.6 Soft Lithography:

Soft Lithography involves the utilization of elastomeric stamps or templates in processes such as microcontact printing and microfluidic patterning to transfer patterns onto a substrate. This flexible and versatile technique facilitates the creation of microscale and nanoscale designs across various materials, offering adaptability and precision in a wide array of applications. For this study, the fabrication of devices was carried out utilizing the optical photolithography technique at the Department of Physics, University of Ulsan as shown in Figure 10.

Optical photolithography consists of the process of applying a light-sensitive substance, referred to as a photoresist (PR), onto a substrate, on which a pattern is transferred using a mask containing transparent and opaque regions. When the patterned mask is brought into close contact with the photoresist-covered substrate, the photoresist undergoes a chemical or physical change. Upon development, the exposed areas of the photoresist reveal the pattern, which can then be subjected to additional treatments such as etching or other processes.

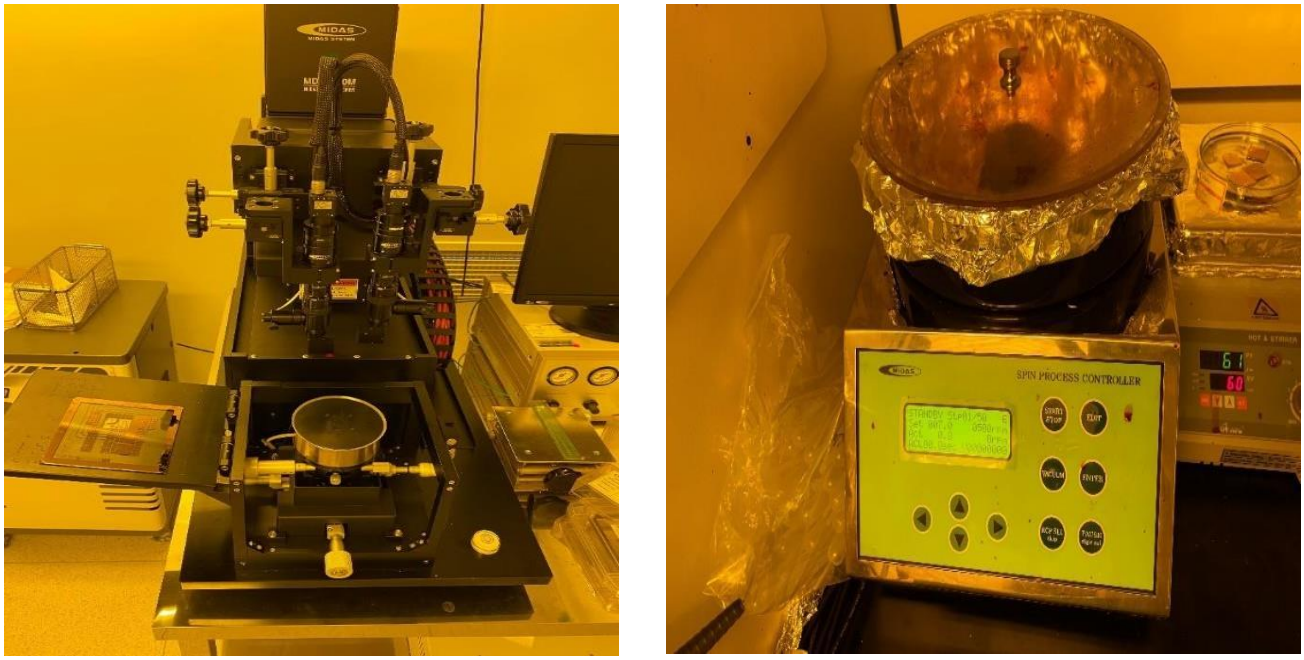

(a) **(b)**

Figure 10. (a) UV Photolithography system and **(b)** Spin Coating

Positive and negative photoresists represent the two primary categories utilized in optical photolithography, each imparting distinct patterns on the substrate due to their differential responses to light exposure and development. In this study, the negative type of photoresists AZ nLOF-2000 is employed. In negative photoresists, the exposed regions serve as the final pattern after development, wherein the more insoluble exposed areas remained, leaving the desired pattern. The photolithography process can be described into the following key steps:

1. Application: Initially, a fine layer of positive photoresist is uniformly applied onto the substrate.

2. Exposure: Subsequently, a mask containing a pattern of transparent and opaque sections is brought into proximity to the photoresist-coated substrate. Light penetrating through the transparent regions induces a chemical transformation in the exposed areas of the photoresist, rendering them more soluble.

3. Development: Following exposure, the photoresist undergoes development, typically involving the use of a specific developer solution. This solution selectively removes the exposed regions of the photoresist, thereby unveiling the desired pattern within the unexposed areas.

By executing these steps, a well-defined photoresist film with the intended shape is formed on the sample surface. This film shields the corresponding areas from ion milling during subsequent processing stages.

3.3 Ion Milling:

Following the photolithography process, the samples are now coated with a precisely shaped thin film of photoresist material. These coated areas play a crucial role in safeguarding the underlying material layers, shielding them from the effects of subsequent ion milling. Conversely, the exposed regions, uncovered during ion milling, gradually degrade over time.

Ion milling stands as a pivotal technology, wielding significant influence in material creation and characterization. This controlled process involves bombarding the sample surface with ions to selectively remove material. Typically, an ion beam, generated from a plasma or accelerator ion source, is focused onto the sample surface.

Sputtering, a widely recognized phenomenon, occurs when ions collide with a surface, transferring kinetic energy to the material's atoms or molecules. This energy transfer leads to the expulsion of atoms or molecules from the surface, resulting in alterations to the surface morphology.

In this study, the ion milling system utilized is the KVET-B2000, sourced from the laboratory for Spin-Orbiton Devices. This setup combines ion milling and sputtering functionalities and is augmented with vacuum system components provided by KOREA VACUUM TECH as shown in Figure 11.

Figure 11. Ion milling system a) power controller, b) cooling system and c) chamber.

The detailed explanation stepwise on how to prepare the ANE devices is as below:

Initially, the deposited substrate was cleaned with Methyl Ethyle ketone and ultrasonicated for 15 minutes. Then, the substrate was blown with the Nitrogen gun. Second, we coat the substrate with AZ nLOF-2000 a negative photoresist at different rotation per minutes values to coat the PR uniformly on the substrate.

In negative photoresist, the final pattern emerges from the exposed areas once the development process eliminates the more soluble regions that were unexposed. Then it was placed on a hot plate at 110 ^{0}C for 180 seconds. During this stage, any unsuitable dust or organic contaminants can be removed.

Then the substrate is exposed to ultraviolet light for 8 seconds to transfer the pattern from the mask to the substrate. After that we bake hard at 120 ^{0}C for 120 seconds and develop for 60 seconds in AZ 300MIF.

By this process we fabricate only the hall bar shaped device, and we repeat the process for fabricating the heater line for the ANE device. The last steps were to deposit heater line using the Magnetron sputtering system. The sequential steps involved are shown in Figure 12.

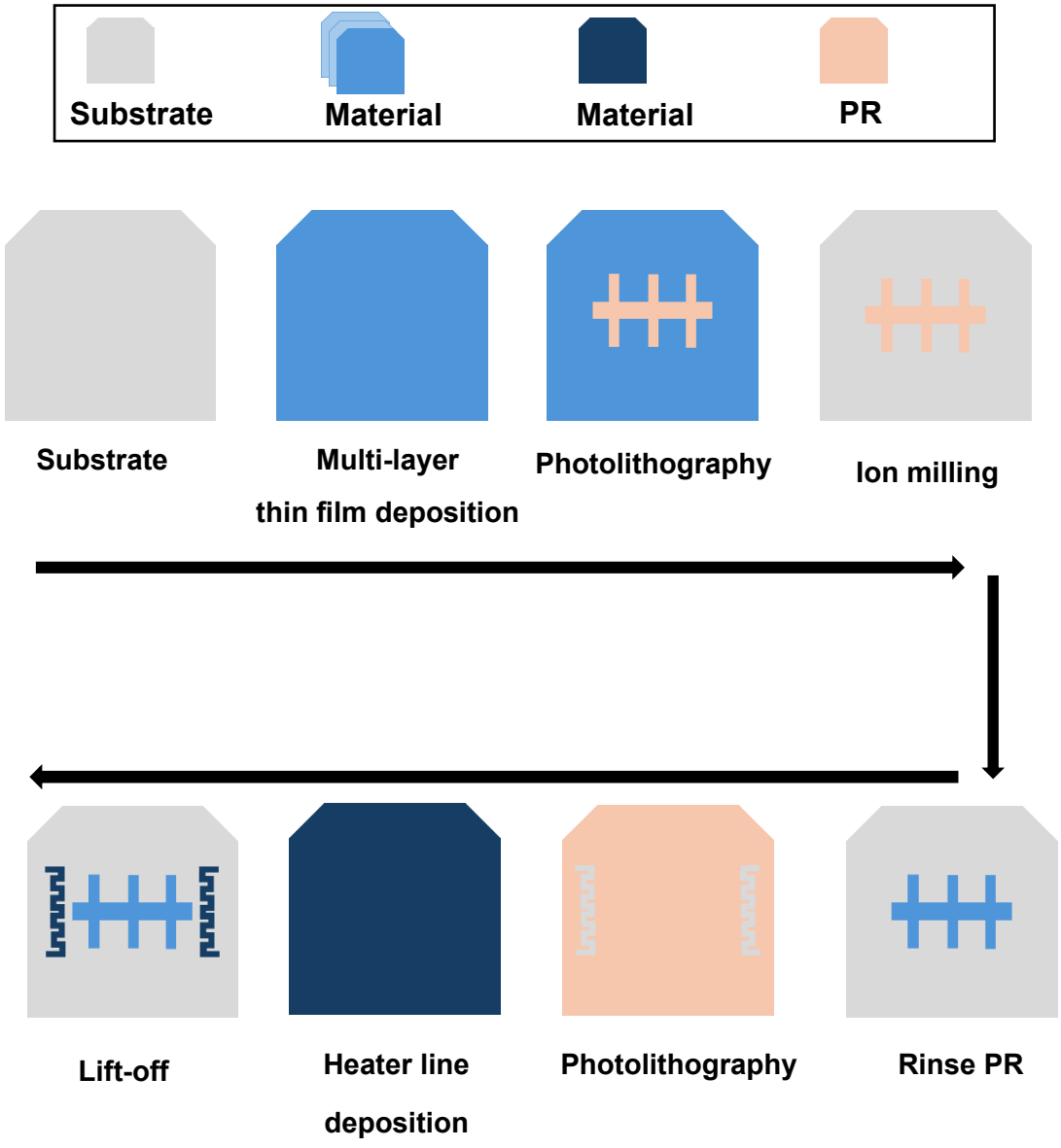

Figure 12. A schematic diagram of device structure through photolithography and ion milling processes

Figure 13 shows the different arrangements of the device at different angles on the MgO (110) substrate for the measurement of anomalous Nernst effect.

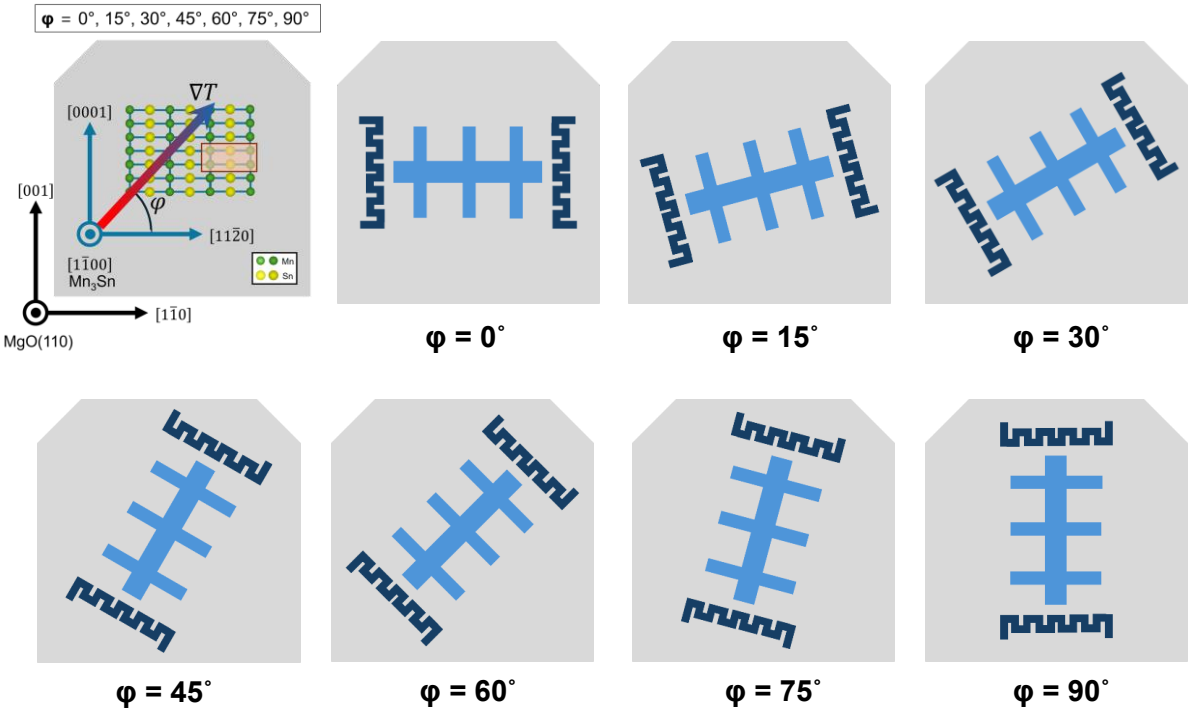

Figure 11. Schematic of anomalous Nernst device on the MgO (110) substrate at different angles.

3.4 X-Ray diffraction (XRD)

X-ray diffraction (XRD) is a valuable tool for analyzing the composition of thin films. When an X-ray beam traverses a crystalline solid, it interacts with the electronic structure of the lattice, resulting in scattering. This scattering occurs due to the periodic arrangement of electrons within the crystal, causing interference among the scattered X-rays, thereby providing insight into the sample's structural properties. It's important to highlight that precise positional information is acquired only when the Bragg law is satisfied given by the following equation:

$$n\lambda = 2d \sin\theta \tag{12}$$

Here, λ denotes the wavelength of the incident X-ray, and d represents the lattice parameter. 2θ signifies the angle between the incident and scattered beams, where n represents the order of the corresponding reciprocal lattice vector.

The XRD experiments conducted in this study employed a Bruker D8 Advanced diffractometer, utilizing Cu Kα radiation (λ = 1.5406 Å), with a 40 kV accelerating voltage and 40 mA current, at the Department of Physics, University of Ulsan as shown in Figure 14. Sample scanning ranged from 20° to 100° in 2θ scale, with an angular step of 0.01°.

Figure 12. XRD measurement system at the Department of Physics, University of Ulsan

To check the crystallinity and quality of the sample we measured the XRD. The XRD pattern of the Mn_3Sn grown on MgO (110) at room temperature is shown in Figure 15. It can be clearly observed that the Mn_3Sn peaks are at $2\theta = 36^0, 58^0 \text{ and } 78^0$ agreed well with the previous work[24].

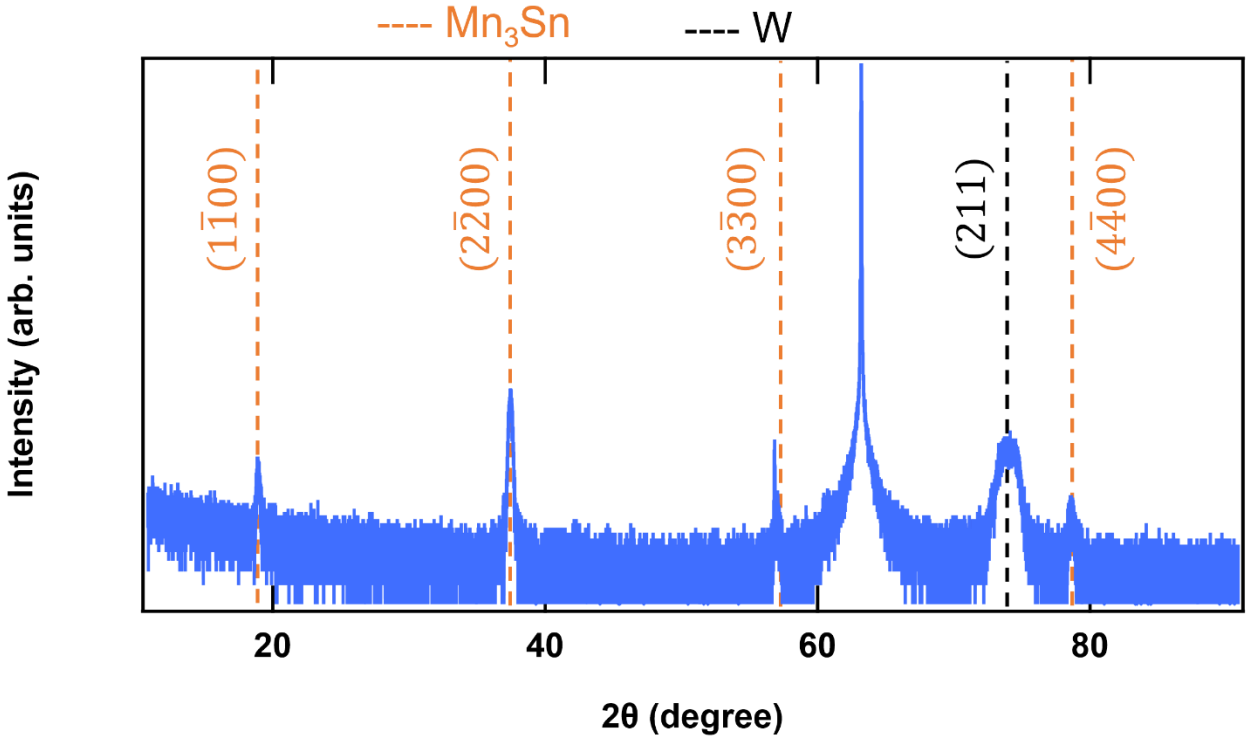

Figure 13. XRD patterns of the sample Mn_3Sn.

4. Results and Discussion

We measured the anomalous Nernst effect (ANE) by applying a current through a Tungsten heater, which was precisely defined using lithography. This generated a thermal gradient in the substrate through the dissipation of Joule heating. By using the on-chip heater method, we could heat one end of the sample relative to the other end by passing current, which can create the temperature gradient.

Anomalous Nernst voltage values from the nearest transversal contacts calculated for different current values through the heater line are given below in Figure 16, which explains the behavior of the ANE. This voltage value increases with increasing the current value. As the current through the heater increases by joule heating increases the temperature gradient across the micro device. We denote the temperature gradient as,

$$\nabla_j T = \frac{\Delta T}{d} \tag{13}$$

Where d is the distance between the two-heater line across the longitudinal side of the hall bar. The temperature difference ΔT is calculated from the heater line at room temperature and the at the high temperature where we apply the current.

To investigate the crystallographic dependance of anomalous Nernst effect, different devices were fabricated at different angles on the MgO (110), as shown schematically in Figure 13. The different angle is labelled as 0˚, 15˚, 30˚, 45˚, 60˚, 75˚, 90˚. Fig. 16 shows the transversal voltage of the devices from the nearest prob to the heater line at different current values applied to the heater for the generation of the temperature gradient. Transversal voltage was measured when an out of plane magnetic field is applied to the devices. It can clearly be observed that the coercivity of the signals decreases with increasing the temperature difference value with the two-heater line. The decrease in coercivity of signals with increasing temperature difference in ANE measurements shows the temperature sensitivity of the Mn_3Sn magnetic properties. Furthermore, we measured the anomalous Hall effect of Mn_3Sn thin film devices. We estimated the total Hall conductivity (σ_{xy}) from the measured Hall resistivity ρ_{yx} and the longitudinal resistivity ρ_{xx} as:

$$\sigma_{xy} = -\frac{\rho_{yx}}{\rho_{xx}^2} \tag{14}$$

The measurement of anomalous Nernst voltage at various angles provides insights into the directional dependence of the ANE in Mn_3Sn. Clear signals for the anomalous Nernst voltage were measured at 0° $[11\bar{2}0]$, 45° $[11\bar{2}3]$, and 90° $[0001]$ suggest specific orientations where the material exhibits pronounced anomalous Nernst behavior. Whereas for the others angles like 15˚, 30˚, 60˚, and 75˚ no significant signals were observed for the anomalous Nernst effect.

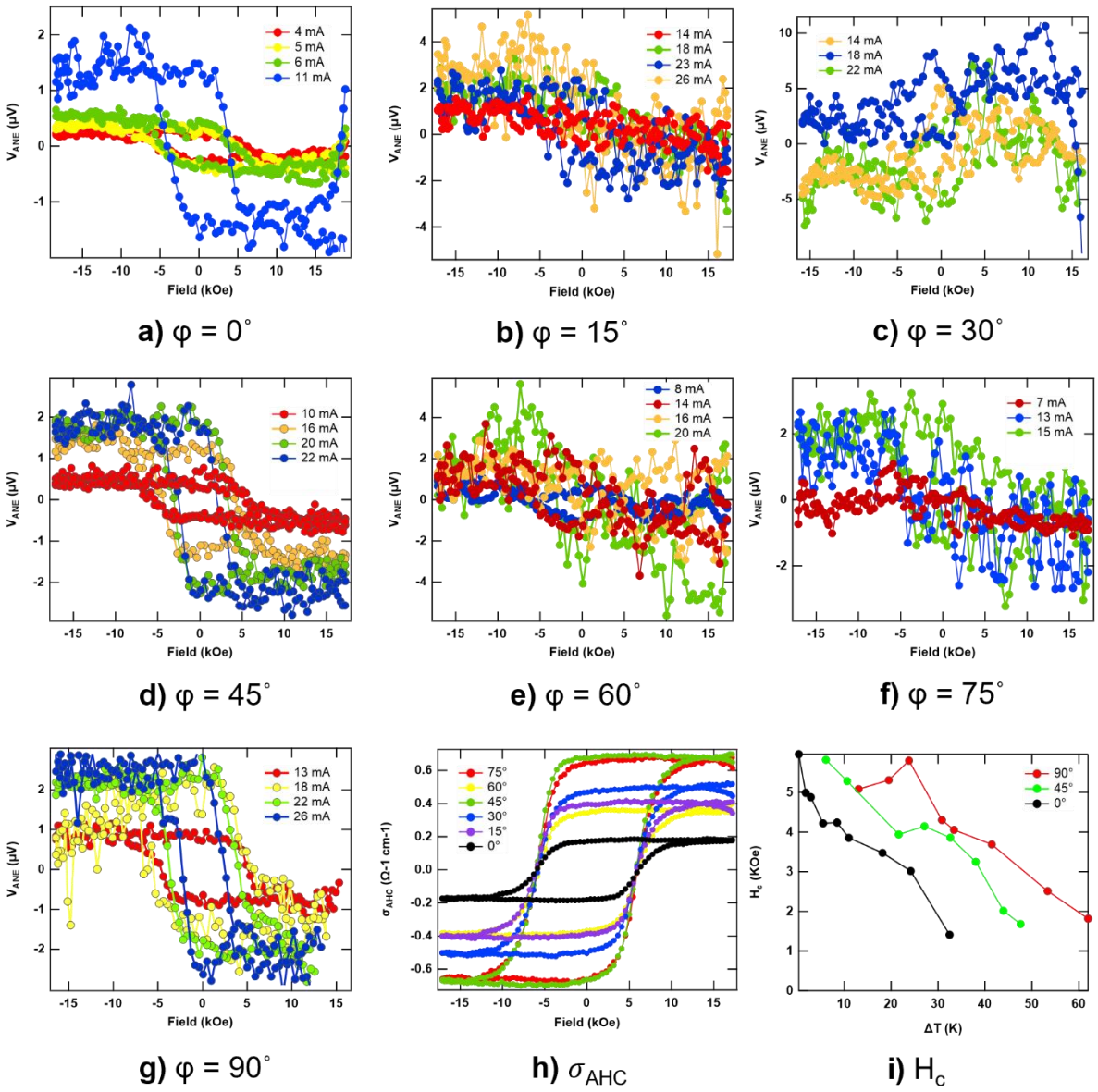

Figure 14. Measurement of the Anomalous Nernst Voltage at different current values along different crystallographic directions.

The resistance of a heater line (or any conductor) typically increases with temperature. This relationship can be mathematically expressed using the following formula:

$$R(T) = R_0\big(1 + \alpha(T - T_0)\big) \tag{15}$$

where $R(T)$ represents the resistance at temperature T. The term R_0 is the resistance at a reference temperature T_0 (25°C), and α is the temperature coefficient of resistance, a material-specific constant. We measured the RT curve for the Tungstun used as a heater line, and it satisfies the condition that the resistance increases with the temperature as shown in Figure 17.

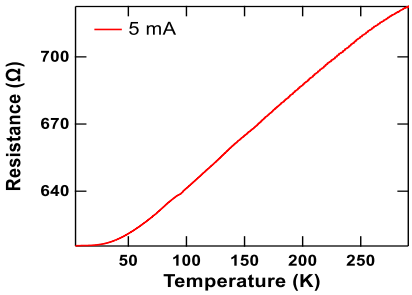

.

Figure 15. Measurement of the resistance vs temperature heater line.

By measuring $R(T)$ the resistance at various temperatures T, I determine how the resistance changes with temperature. Using these measurements, I calculated the temperature coefficient of resistance α for this specific heater line, finding it to be 0.00063 °C^{-1}. This value indicates the rate at which the resistance increases per degree Celsius rise in temperature. After finding the temperature coefficient of resistance for the specific heater line dimensions, we calculated the amount of temperature produced by the heater line from the amount of resistance increase from the initial resistance. The anomalous Nernst voltage along 0° $[11\bar{2}0]$, 45° $[11\bar{2}3]$, and 90° $[0001]$ is increasing linearly with increasing the current value of the heater line as shown in Figure 18 (a).

(a) **(b)**

Figure 16. a) Measurement of the Anomalous Nernst Voltage at *0°, 45°, and 90°* at different current values, **b)** The Anomalous Nernst Coefficient vs Temperature.

Finally, we calculated the value for the anomalous Nernst coefficient value for the thin film of Mn_3Sn for the crystallographic direction of $[11\bar{2}0]$, $[11\bar{2}3]$, and $[0001]$ through the given equation (10) and Fig.18 (b) shows the ANE coefficient value for the different direction at corresponding temperature difference value between the two-heater line.

$$\Delta S_{ij} = \frac{\Delta V_i}{\Delta T} \tag{16}$$

As the temperature difference increases the ANE coefficient value decreases as calculated by the pervious works in the bulk Mn_3Sn [25].

Table 1. Represents the ANE coefficient values for the device along $[11\bar{2}0]$.

Current(mA)	ΔV (μV)	ΔT(K)	ΔS_{ij} (μV/K)
5	0.65	1.78	0.43
6.5	1.09	3.68	0.35
11	2.76	10.98	0.29
14.5	4	19.68	0.20
16	5.3	26.8	0.19

Table 2. Represents the ANE coefficient values for the device along $[11\bar{2}3]$.

Current(mA)	ΔV (μV)	ΔT(K)	ΔS_{ij} (μV/K)
5	0.235	1.1983	0.20
10	1.16	10.6211	0.11
16	2.2	27.0868	0.08
20	3.59	38.0388	0.09
22	4.4	43.9175	0.10

Table 3. Represents the ANE coefficient values for the device along $[0001]$.

Current(mA)	ΔV (μV)	ΔT(K)	ΔS_{ij} (μV/K)
14	2.13	15.2784	0.14
18	3.09	23.7986	0.13
21	3.16	30.8117	0.10
22	3.82	33.3915	0.11
26	4.91	53.3457	0.09

5. Conclusion

In conclusion the Nernst coefficient S_{ij} for bulk Mn_3Sn has been reported to lie within the range of 0.3 to 0.6 μV/K across a temperature interval of 200-250 K. By fabricating thin films of Mn_3Sn the Nernst coefficient S_{ij} for the different crystallographic directions $[11\bar{2}0]$, $[11\bar{2}3]$, and $[0001]$ is 0.43, 0.2, and 0.14 respectively. These calculated values are slightly lower than the previously reported bulk values for Mn_3Sn but remain within the same order of magnitude, indicating consistent behavior across different crystallographic orientations.

Epitaxially grown Mn_3Sn thin films exhibit a temperature-dependent decrease in the anomalous Nernst Coefficient. Observation suggests that thin film magneto-thermoelectric properties may differ from bulk, possibly influenced by film growth and structure. Unlike conventional thermoelectric devices, Anomalous Nernst devices eliminate the need for p-type and n-type materials, simplifying technological integration. This work not only highlights the development of multi-terminal devices but also expands the understanding of Anomalous Nernst Effect in antiferromagnetic materials which leads to the future innovations and applications in energy harvesting and memory devices.

References:

[1] K. Behnia, “The Nernst effect and the boundaries of the Fermi liquid picture,” *Journal of Physics: Condensed Matter*, vol. 21, no. 11, p. 113101, Mar. 2009, doi: 10.1088/0953-8984/21/11/113101.

[2] T. J. Seebeck, “Ueber die magnetische Polarisation der Metalle und Erze durch Temperatur-Differenz,” *Ann Phys*, vol. 82, no. 2, pp. 133–160, Jan. 1826, doi: 10.1002/andp.18260820202.

[3] M. and P. V. Dyakonov, “Possibility of Orienting Electron Spins with Current,” *Soviet Journal of Experimental and Theoretical Physics Letters*, vol. 13, p. 467, May 1971.

[4] H. Kontani, T. Tanaka, D. S. Hirashima, K. Yamada, and J. Inoue, “Giant Orbital Hall Effect in Transition Metals: Origin of Large Spin and Anomalous Hall Effects,” *Phys Rev Lett*, vol. 102, no. 1, p. 016601, Jan. 2009, doi: 10.1103/PhysRevLett.102.016601.

[5] T. Tanaka *et al.*, “Intrinsic spin Hall effect and orbital Hall effect in transition metals,” *Phys Rev B*, vol. 77, no. 16, p. 165117, Apr. 2008, doi: 10.1103/PhysRevB.77.165117.

[6] D. Go, D. Jo, C. Kim, and H.-W. Lee, “Intrinsic Spin and Orbital Hall Effects from Orbital Texture,” *Phys Rev Lett*, vol. 121, no. 8, p. 086602, Aug. 2018, doi: 10.1103/PhysRevLett.121.086602.

[7] S. Ding *et al.*, “Harnessing Orbital-to-Spin Conversion of Interfacial Orbital Currents for Efficient Spin-Orbit Torques,” *Phys Rev Lett*, vol. 125, no. 17, p. 177201, Oct. 2020, doi: 10.1103/PhysRevLett.125.177201.

[8] D. Jo, D. Go, and H.-W. Lee, “Gigantic intrinsic orbital Hall effects in weakly spin-orbit coupled metals,” *Phys Rev B*, vol. 98, no. 21, p. 214405, Dec. 2018, doi: 10.1103/PhysRevB.98.214405.

[9] S. Nakatsuji, N. Kiyohara, and T. Higo, “Large anomalous Hall effect in a non-collinear antiferromagnet at room temperature,” *Nature*, vol. 527, no. 7577, pp. 212–215, Nov. 2015, doi: 10.1038/nature15723.

[10] M. Ikhlas *et al.*, “Large anomalous Nernst effect at room temperature in a chiral antiferromagnet,” *Nat Phys*, vol. 13, no. 11, pp. 1085–1090, Nov. 2017, doi: 10.1038/nphys4181.

[11] C. Wuttke *et al.*, “Berry curvature unravelled by the anomalous Nernst effect in <math> <msub> <mi>Mn</mi> <mn>3</mn> </msub> <mi mathvariant="normal">Ge</mi> </math>,” *Phys Rev B*, vol. 100, no. 8, p. 085111, Aug. 2019, doi: 10.1103/PhysRevB.100.085111.

[12] A. Ghosh, A. Chanda, and R. Mahendiran, “Anomalous Nernst effect in Pr0.5Sr0.5CoO3,” *AIP Adv*, vol. 11, no. 3, Mar. 2021, doi: 10.1063/5.0039709.

[13] “ANE in Mn3NiN thin films”.

[14] H. Narita, T. Higo, M. Ikhlas, S. Nakatsuji, and Y. Otani, “Effect of sample size on anomalous Nernst effect in chiral antiferromagnetic Mn3Sn devices,” *Appl Phys Lett*, vol. 116, no. 7, Feb. 2020, doi: 10.1063/1.5126615.

[15] F. Caglieris *et al.*, “Anomalous Nernst effect and field-induced Lifshitz transition in the Weyl semimetals TaP and TaAs,” *Phys Rev B*, vol. 98, no. 20, p. 201107, Nov. 2018, doi: 10.1103/PhysRevB.98.201107.

[16] Y. Pu, D. Chiba, F. Matsukura, H. Ohno, and J. Shi, “Mott Relation for Anomalous Hall and Nernst Effects in Ferromagnetic Semiconductors,” *Phys Rev Lett*, vol. 101, no. 11, p. 117208, Sep. 2008, doi: 10.1103/PhysRevLett.101.117208.

[17] D. Xiao, M.-C. Chang, and Q. Niu, “Berry phase effects on electronic properties,” *Rev Mod Phys*, vol. 82, no. 3, pp. 1959–2007, Jul. 2010, doi: 10.1103/RevModPhys.82.1959.

[18] D. Xiao, Y. Yao, Z. Fang, and Q. Niu, “Berry-Phase Effect in Anomalous Thermoelectric Transport,” *Phys Rev Lett*, vol. 97, no. 2, p. 026603, Jul. 2006, doi: 10.1103/PhysRevLett.97.026603.

[19] H. Yang, Y. Sun, Y. Zhang, W.-J. Shi, S. S. P. Parkin, and B. Yan, “Topological Weyl semimetals in the chiral antiferromagnetic materials Mn_3Ge and Mn_3Sn,” *New J Phys*, vol. 19, no. 1, p. 015008, Jan. 2017, doi: 10.1088/1367-2630/aa5487.

[20] Y. P. Mizuta and F. Ishii, “Contribution of Berry Curvature to Thermoelectric Effects,” in *Proceedings of the International Conference on Strongly Correlated Electron Systems (SCES2013)*, Journal of the Physical Society of Japan, Jun. 2014. doi: 10.7566/JPSCP.3.017035.

[21] Y. P. Mizuta and F. Ishii, “Large anomalous Nernst effect in a skyrmion crystal,” *Sci Rep*, vol. 6, no. 1, p. 28076, Jun. 2016, doi: 10.1038/srep28076.

[22] D. Xiao, Y. Yao, Z. Fang, and Q. Niu, “Berry-Phase Effect in Anomalous Thermoelectric Transport,” *Phys Rev Lett*, vol. 97, no. 2, p. 026603, Jul. 2006, doi: 10.1103/PhysRevLett.97.026603.

[23] J. A. Liddle and G. M. Gallatin, “Nanomanufacturing: A Perspective,” *ACS Nano*, vol. 10, no. 3, pp. 2995–3014, Mar. 2016, doi: 10.1021/acsnano.5b03299.

[24] J.-Y. Yoon *et al.*, “Correlation of anomalous Hall effect with structural parameters and magnetic ordering in Mn3+ *x* Sn1− *x* thin films,” *AIP Adv*, vol. 11, no. 6, Jun. 2021, doi: 10.1063/5.0043192.

[25] M. Ikhlas *et al.*, “Large anomalous Nernst effect at room temperature in a chiral antiferromagnet,” *Nat Phys*, vol. 13, no. 11, pp. 1085–1090, Nov. 2017, doi: 10.1038/nphys4181.